J. Fluid Mech. (2014), *vol.* 749, *pp.* 818–840.
doi:10.1017/jfm.2014.249

Spatial organization of large- and very-large-scale motions in a turbulent channel flow

Jin Lee[1], Jae Hwa Lee[1], Jung-Il Choi[2] and Hyung Jin Sung[1],†

[1]Department of Mechanical Engineering, KAIST, 291 Daehak-ro, Yuseong-gu, Daejeon 305-701, Korea

[2]Department of Computational Science and Engineering, Yonsei University, 50 Yonsei-ro, Seodaemun-gu, Seoul 120-749, Korea

(Received 19 November 2013; revised 17 March 2014; accepted 1 May 2014; first published online 23 May 2014)

Direct numerical simulations were carried out to investigate the spatial features of large- and very-large-scale motions (LSMs and VLSMs) in a turbulent channel flow ($Re_\tau = 930$). A streak detection method based on the streamwise velocity fluctuations was used to individually trace the cores of LSMs and VLSMs. We found that both the LSM and VLSM populations were large. Several of the wall-attached LSMs stretched toward the outer regions of the channel. The VLSMs consisted of inclined outer LSMs and near-wall streaks. The number of outer LSMs increased linearly with the streamwise length of the VLSMs. The temporal features of the low-speed streaks in the outer region revealed that growing and merging events dominated the large-scale (1–3δ) structures. The VLSMs ($>3\delta$) were primarily created by merging events, and the statistical analysis of these events supported that the merging of large-scale upstream structures contributed to the formation of VLSMs. Because the local convection velocity is proportional to the streamwise velocity fluctuations, the streamwise-aligned structures of the positive- and negative-u patches suggested a primary mechanism underlying the merging events. The alignment of the positive- and negative-u structures may be an essential prerequisite for the formation of VLSMs.

Key words: boundary layer structure, turbulence simulation, turbulent boundary layers

1. Introduction

In wall-bounded turbulent flows, vortical structures have been classified as hairpin vortices or large-scale structure in hairpin packets, depending on the relevant spatial characteristics (Adrian, Meinhart & Tomkins 2000). Kim & Adrian (1999) first observed the presence of very-large-scale motions (VLSMs) in turbulent pipe flows. After their observation, the significance and influence of VLSMs on turbulent flows were recognized by a variety of researchers. The presence of VLSMs or superstructures in other flow types has been observed; for instance, Monty *et al.* (2007) examined such structures in pipe flows, and Lee & Sung (2011) examined such structures in turbulent boundary layers (TBLs). Because turbulent motions

† Email address for correspondence: hjsung@kaist.ac.kr

are enhanced by the kinetic energy of the largest-scale features, the importance of VLSMs may be appreciated by considering the kinetic energy present in the outer region (Pope 2000). The dominance of VLSMs in a turbulent flow increases with the Reynolds number (Marusic, Mathis & Hutchins 2010; Smits, McKeon & Marusic 2011; Hultmark *et al.* 2012); therefore, an understanding of the roles of VLSMs is required in several application areas.

VLSMs, as the name suggests, are distinguished from large-scale motions (LSMs) by the streamwise extent of their low-speed regions. The large streamwise extents of VLSMs increase the long-wavelength energy portion of the premultiplied energy spectra of streamwise velocity fluctuations (Monty *et al.* 2009). Because the area enclosed by such energy spectra represents the streamwise normal stresses (Marusic *et al.* 2010), the increased value of the energy spectra in a high-Reynolds-number flow is directly correlated with the large streamwise normal stresses in the outer region. In particular, the streamwise turbulent energy of the large wavelength increases significantly in the outer regions (Hoyas & Jiménez 2006; Monty *et al.* 2009; Schlatter *et al.* 2010) and contribute to the outer peak of a spectrum. The VLSMs produce energetic turbulent motions in the outer regions of their structures. The presence of an outer peak was observed in the streamwise normal stress profile obtained from an experimental measurement of a pipe flow (Morrison *et al.* 2004; Hultmark *et al.* 2012); however, the higher energies in the outer regions of the structures may have arisen from experimental artifacts (Kim 2012). Notwithstanding the emergence of nanoscale anemometry probes (Bailey *et al.* 2010; Vallikivi *et al.* 2011), the observation of VLSMs are not totally free from experimental artifacts of both the probe size and the Taylor's frozen turbulence hypothesis. Moreover, the detection of VLSMs is mostly based on the time-averaged quantities; for example, the premultiplied energy spectra (Kim & Adrian 1999; Monty *et al.* 2009), the two-point correlation of the streamwise velocity fluctuations (Monty *et al.* 2007; Lee & Sung 2013) and the proper orthogonal decomposition (Baltzer, Adrian & Wu 2013). Thus, there is a growing concern on further investigation of VLSMs by numerical simulation with a temporal analysis.

VLSMs are characterized by the presence of strong Reynolds stresses in a fluid structure. Guala, Hommema & Adrian (2006) and Balakumar & Adrian (2007) showed that VLSMs contain 50–60 % of the cumulative energy fraction of the Reynolds shear stress. Ganapathisubramani, Longmire & Marusic (2003) reported that VLSMs have a large influence on the turbulence statistics. Little work has been performed toward examining the role of VLSMs in the local behaviour of turbulence statistics. Decomposing the contributions of VLSMs to the secondary peak of the streamwise normal stress can provide some insight into the formation of the secondary peak in very-high-Reynolds-number flows. Although these results supported the presence of VLSMs, the mechanism by which VLSMs form remains under debate. Two major driving forces have been proposed as underlying the VLSM formation mechanism, based on (i) the concatenation of large-scale structures (Kim & Adrian 1999; Guala *et al.* 2006; Lee & Sung 2011), or (ii) the effects of linear stability (McKeon & Sharma 2010; Hellström, Sinha & Smits 2011). The first hypothesis was tested by measuring the fluctuations in the convection velocity in a hairpin packet model (Adrian *et al.* 2000). Older and larger packets are characterized by weak negative streamwise velocity fluctuations; therefore, they were expected to move faster than the younger and smaller packets. These studies suggested that the merging events provided the primary mechanism of VLSM formation. Support for this hypothesis was provided by the observation of a meandering feature in the superposition of nearly all of the energetic modes.

The existence of VLSMs was initially identified by examining the wavenumber space. The footprints of VLSMs in physical space were detected across large spatial dimensions. Contrary to expectations based on the original definition of VLSMs, which focused on the streamwise velocity fluctuations, Ganapathisubramani *et al.* (2003) and Lee & Sung (2011) identified large and very large negative streamwise fluctuating structures characterized by strong Reynolds shear stress events and vortical structures in a wall-parallel plane, namely, the feature extraction algorithm. They examined the spatial features around hairpin vortices because LSMs and VLSMs were believed to be created by the alignment of hairpin vortices to create strong second-quadrant Reynolds shear stresses inside the hairpins. Dennis & Nickels (2011*b*) carried out a statistical investigation to examine the features of VLSMs and revealed that low-speed streaks were generally found a distance of up to 7δ along the streamwise direction. It should be noted, however, that this study employed the Taylor frozen hypothesis, which may overestimate the streamwise extent by neglecting diffusion effects.

The statistical properties of VLSMs, including the number of structures measured as a function of the spatial extent, were studied by several research groups (Ganapathisubramani *et al.* 2003; Dennis & Nickels 2011*b*; Baltzer *et al.* 2013), who showed that very long structures identified by the negative streamwise velocity fluctuations were apparent in the log layer. The very-long structures contributed significantly to the Reynolds shear stress. If the formation of a VLSM were related to multiple LSMs, statistical evidence supporting a relationship between the LSMs and the packet structures with very long structures would be required. Additional information may be obtained by examining the LSM and VLSM populations in a real three-dimensional (3D) flow field.

The instantaneous visualizations of multiple LSMs in a VLSM were demonstrated (Hutchins & Marusic 2007; Lee & Sung 2011; Dennis & Nickels 2011*b*). Although Lee & Sung (2011) provided evidence in support of the formation mechanism using time-evolving instantaneous flow fields with a small number of visualizations, they did not provide a statistical analysis of the formation frequency. A statistical approach would be required to understand the formation mechanism based on relevant events. The temporal changes in the turbulence structures have been examined in many studies by tracking individual structures. The positions and shapes of time-evolving structures may be traced by extracting the hairpin vortex and the vortex packet from the flow field (Dennis & Nickels 2011*a*; Elsinga *et al.* 2012). The temporal analysis results identified a merging process among individual vortices and packet organization. Nolan & Zaki (2013) detected quasi-streamwise streaky structures based on the local maximum of streamwise velocity fluctuations. Although their method was used to detect laminar streaks in a transitional boundary layer, their study suggested a possible extension to the extraction of LSMs and VLSMs in fully turbulent flows.

The objective of the present study was to explore the population-level properties of LSMs and VLSMs and to obtain statistical evidence in support of a VLSM formation mechanism. The present study investigated the contribution of VLSMs, distinct from the contribution of the LSMs, to the turbulence statistics. To do so, we performed direct numerical simulations of a fully developed turbulent channel flow at $Re_\tau = 930$ with a long streamwise domain ($10\pi\delta$). The streak detection method (Dennis & Nickels 2011*b*; Nolan & Zaki 2013) was modified for the detection and tracking of LSMs and VLSMs. The population-level properties of both structures were examined statistically and evaluated using the detection methods described below. The spatial and temporal relationships between the LSMs and VLSMs were examined.

Statistical evidence supporting the mechanism by which the streamwise-aligned LSMs connected within the VLSMs was obtained. The temporal information suggested a possible scenario involving the merging events.

2. Numerical details

2.1. *Dataset obtained using direct numerical simulations*

The 3D flow fields in a very long streamwise domain were obtained by simulating a fully developed turbulent channel flow using direct numerical simulations. The Navier–Stokes equation and the continuity equation were used as the governing equations:

$$\frac{\partial \tilde{u}_i}{\partial t} + \frac{\partial}{\partial x_j}\tilde{u}_i\tilde{u}_j = -\frac{\partial \tilde{p}}{\partial x_i} + \frac{1}{Re}\frac{\partial}{\partial x_j}\frac{\partial \tilde{u}_i}{\partial x_j} \tag{2.1}$$

$$\frac{\partial \tilde{u}_i}{\partial x_i} = 0 \quad (\tilde{u}_i = U_i + u_i). \tag{2.2}$$

Here, all terms were normalized by the channel half-height (δ) and the laminar centreline velocity (U_{CL}). The Reynolds number ($Re \equiv U_{CL}\delta/\nu$) is 28 000, which corresponded to the friction Reynolds number $Re_\tau = 930$. Uppercase symbols refer to mean quantities and lowercase symbols are reserved for fluctuations. In the present study, x, y and z denote the streamwise, wall-normal and spanwise directions, respectively. The governing equations were solved using the fully implicit decoupling method of Kim, Baek & Sung (2002). All terms were discretized using the Crank–Nicolson method in time and the second-order central difference scheme in space. Both the temporal and spatial discretizations were performed with second-order accuracy. Periodic boundary conditions were applied in the x and z directions. No-slip boundary conditions were used on the bottom and top walls.

The very long structures were inspected using a sufficiently long streamwise domain to avoid artificial domain effects in the LSMs and VLSMs (Simens *et al.* 2009). Thus, in the present study, the domain size ($L_x \times L_y \times L_z$) was set to $10\pi\delta \times 2\delta \times 3\pi\delta$, which is similar to the domain used by Hoyas & Jiménez (2006) except that the streamwise extent differed. A staggered grid system was applied in the flow field simulation across $4993(x) \times 401(y) \times 2497(z)$ (almost 5 billions) grid points. A uniform grid spacing was used in the wall-parallel (x and z) directions, while non-uniform grid was used in the wall-normal (y) direction. The spatial resolution was $\Delta x^+ = 5.86$, $\Delta y^+_{\min} = 0.0287$, $\Delta y^+_{\max} = 7.31$ and $\Delta z^+ = 3.51$, which was relatively fine and improved the spatial accuracy. Here, the superscript $+$ indicates that the quantities were normalized by the friction velocity (u_τ), and the capital letters indicate the temporally and spatially averaged statistics. The simulation was carried out using 1536 cores on a Tachyon II (SUN X6275) KISTI supercomputer. The time step was $0.002\delta/U_{CL}$, which corresponded to $\Delta t^+ = 0.0618$. The total averaging time was $220\delta/U_{CL}$, which corresponded to seven sweeps across the whole bulk flow domain. A total of 2010 snapshots were collected in time step intervals of $0.1\delta/U_{CL}$. As shown in figure 1, the profile of the mean streamwise velocity is in qualitatively good agreement with that of Hoyas & Jiménez (2006), while the profile shows a slight deviation in the core region. The profiles of the Reynolds stresses agreed well with those of Hoyas & Jiménez (2006).

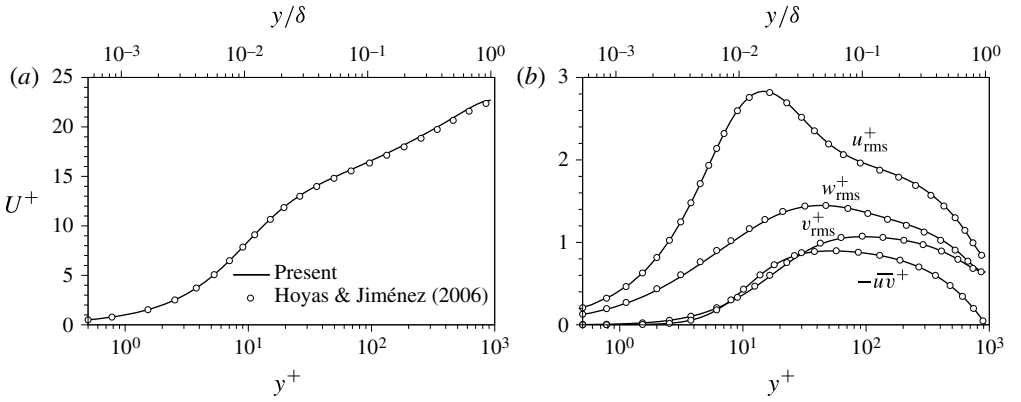

FIGURE 1. Turbulence statistics: (*a*) mean streamwise velocity; (*b*) turbulence intensities and the Reynolds shear stress.

2.2. *Streak detection*

Both the LSMs and VLSMs were visualized based on the streamwise-elongated volumes associated with the negative u (Dennis & Nickels 2011*a*,*b*; Lee & Sung 2011; Baltzer *et al.* 2013). The observation of a low-speed region in the 3D flow field characterized by a velocity fluctuation that exceeded a threshold value was accompanied by the appearance of several isosurfaces that formed a complex shape. The appearance of complex shapes, due to small-scale motions that interacted with LSMs, interrupted the detection processes (Dennis & Nickels 2011*b*). Hence, the extraction of characteristic lines demarcating the LSMs and VLSMs were more helpful toward investigating the time evolution and statistics. Long structures were detected in the present study using a detection algorithm based on identifying the local maximum of the streamwise velocity fluctuations (Nolan & Zaki 2013). To exclude small-scale motions in high-Reynolds-number turbulent flows, a smoothing filter must be adopted to exclude any small-scale features (Hutchins & Marusic 2007).

Figure 2 illustrates an extraction procedure implemented in the present study. A sample instantaneous flow field is visualized in figure 2(*a*). Prior to visualizing the isosurface of the velocity fluctuations, it is strongly recommended that a reasonable threshold be selected (del Álamo *et al.* 2006). Consistent with previous reports (Dennis & Nickels 2011*b*; Baltzer *et al.* 2013), the threshold used to identify the low-momentum region was carefully chosen to be 10 % of the bulk velocity (U_b), i.e. $u_{th,raw} = 0.1U_b$. The detailed procedure involved in the preparation and extraction methods for the low- and high-speed structures, i.e. u-structures, is described as follows.

Step 1: *Gaussian filter*. In the instantaneous flow field of u (figure 2*a*), the small-scale features of u were attenuated in the spanwise and wall-normal planes using the Gaussian filter. A 2D Gaussian filter in the cross-stream plane was applied to the standard deviation as a function of the wall-normal location $\sigma(y)$ because the average spanwise dimension of the u-structures varied with y. Here, the standard deviation was determined by the half-width of the two-point correlation function of the threshold of $R_{uu} = 0.5$ in the spanwise direction in order to prevent adjacent low-speed streaks from counterbalancing high-speed streaks. The curve-fitted standard deviations of the half-width of R_{uu} at 13 wall-normal positions were used to generate the filter

$$\sigma(y/\delta) = 0.1513(y/\delta)^3 - 0.5142(y/\delta)^2 + 0.4992(y/\delta) + 0.0176. \tag{2.3}$$

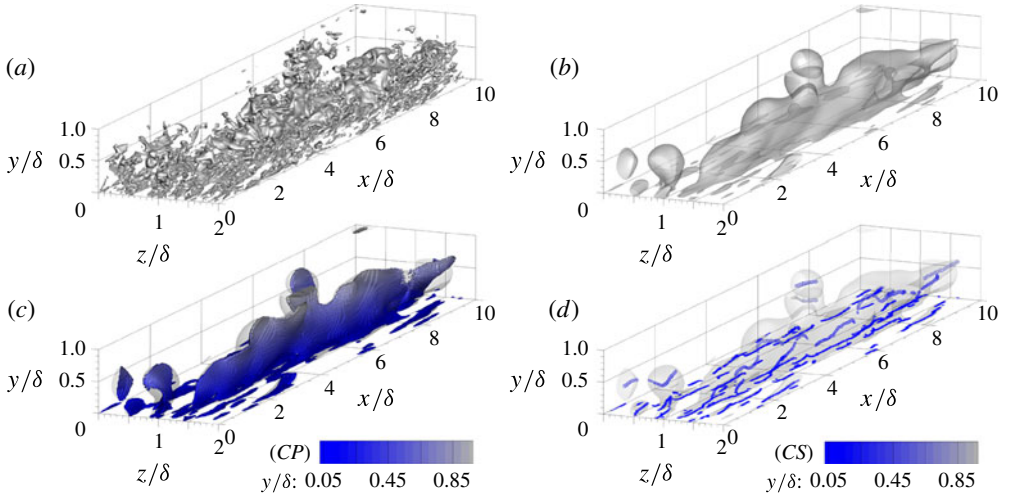

FIGURE 2. (Colour online) Isosurfaces of (*a*) the streamwise velocity fluctuations (light grey contours) u, visualized using $u/U_b = -0.10$ $(= -u_{th,raw})$ and (*b*) the Gaussian $(\sigma(y))$ and long-wavelength-pass filtered $(>1\delta)$ flow field $\hat{u}$, visualized using $\hat{u} = -u_{th}$. The positions of the local extrema of the negative $-u$ (*c*) in the z direction (*CP*) and (*d*) in the yz (cross-stream) plane (*CS*) from the filtered image ($\hat{u}$, transparent grey isosurface) are shown as dark grey (blue online) contours. See the supplementary movie available at http://dx.doi.org/10.1017/jfm.2014.249.

Note that the influence of the standard deviations on the detection is compared in § A.1.

Step 2: *long-wavelength-pass filter*. A long-wavelength-pass filter was applied to the Gaussian-filtered fields to extract out structures longer than 1δ in the streamwise direction. This value was the same cutoff value used by Mathis, Hutchins & Marusic (2009) to compute the amplitude modulation. A sample of an isosurface of the 10δ-long structure is shown in the filtered u-field $\hat{u}$ (figure 2*b*). Because the velocity fluctuations were weakened by the two filters, the isosurface shown in figure 2(*b*) was visualized using the threshold $u_{th}(y) = f(y)u_{th,raw}$. Here, the factor $f(y)$ was defined by the ratio of the correlation function, $f(y) = \langle u(y)\hat{u}(y)\rangle / \langle u(y)u(y)\rangle$. Note that the influence of the threshold level on the detection is compared in § A.2.

Step 3: *structure detection*. The filtered field $\hat{u}$ yielded the quasi-vertical characteristic planes (*CP*) that represented the streamwise and wall-normal dimensions of the u-structure, as seen in figure 2(*c*). The *CP* were obtained from the local extrema of the filtered field in the z direction;

$$CP = \begin{cases} 1 & \text{where } \partial\hat{u}/\partial z = 0 \text{ and } \hat{u} > u_{th}, \\ -1 & \text{where } \partial\hat{u}/\partial z = 0 \text{ and } \hat{u} < -u_{th}, \\ 0 & \text{otherwise.} \end{cases} \tag{2.4}$$

By using *CP*, for example, the u-structure in the sample instantaneous flow field (figure 2*a*) easily turned out a 10δ-long structure. Next, the characteristic spines (*CS*) were extracted from the quasi-vertical shape of *CP* by using the local extrema in the vertical direction ($\partial\hat{u}/\partial\eta = 0$; η is the vertical direction on *CP*), as seen in figure 2(*d*).

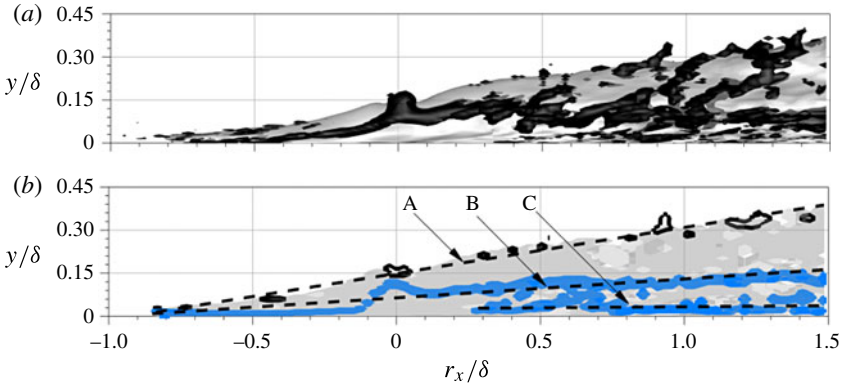

FIGURE 3. (Colour online) Linearly estimated velocity field of a spanwise vortex $\langle u_i(r_x, y, r_z)|\lambda_2^{xy}(x, y_{ref}, z)\rangle$ at $y_{ref}/\delta = 0.15$ (side view). (*a*) The vortices (black) and negative streamwise velocity (light grey) are denoted by an isosurface of $\lambda_2\delta^2/U_{CL}^2 = -50$ and $u/\sqrt{u^2+v^2+w^2} = -0.5$. (*b*) The dark grey (blue online) line and light grey plane indicate the characteristic spines (*CS*) and the characteristic quasi-vertical planes (*CP*) of the negative-u.

The detection of *CS* is obtained from the local extrema of the filtered field in the streamwise plane:

$$CS = \begin{cases} 1 & \text{where } \partial\hat{u}/\partial z = \partial\hat{u}/\partial y = 0 \text{ and } \hat{u} > u_{th}, \\ -1 & \text{where } \partial\hat{u}/\partial z = \partial\hat{u}/\partial y = 0 \text{ and } \hat{u} < -u_{th}, \\ 0 & \text{otherwise.} \end{cases} \tag{2.5}$$

As shown in figure 2(*d*), several δ-long *CS* strings are situated in the 10δ-long u-structure in the sample instantaneous flow field (figure 2*a*).

The present detection method can be used for both positive- and negative-u regions. In order to scrutinize the formation of very-long low-speed structures, the negative-u region is focused on hereafter. The physical meaning of *CS* can be deduced from a stochastic estimation of the conditionally averaged velocity fields around a spanwise vortex $\langle u_i(r_x, y, r_z)|\lambda_2^{xy}(x, y_{ref}, z)\rangle$, as shown in figure 3. The stochastic estimation method is described in detail by Lee *et al.* (2013). Note that the spanwise vortices λ_2^{xy} were identified from the velocity gradient tensor in the xy plane using λ_2. Here λ_2 is the second largest eigenvalue of the tensor $\boldsymbol{S}_{ik}\boldsymbol{S}_{kj} + \boldsymbol{\Omega}_{ik}\boldsymbol{\Omega}_{kj}$, where $\boldsymbol{S}_{ij}$ is the symmetric component and Ω_{ij} is the antisymmetric component of the velocity gradient tensor (Jeong & Hussain 1995). Several hairpin vortices (black in figure 3*a*) were observed around the reference positions. Because a strong backward motion occurred beneath the spanwise vortex (a head of the hairpin vortex) in the outer region, the *CS* core (dark grey (blue online) in figure 3*b*) represents the characteristic spine of a hairpin vortex packet. The wall-normal location of the *CS* core increased with the streamwise direction (marked line 'B') and was approximately proportional to the growth rate of the packet (marked line 'A'). The *CS* core represented the shoulder line of the packet. A *CS* core near the wall was observed and may have been induced by the hairpin legs (marked line 'C'). The *CP* core (light grey in figure 3*b*) displayed a quasi-vertical plane of the low-momentum region. Therefore, the *CS* core and *CP* core indicated the spatial extents of the hairpin packet and the streamwise

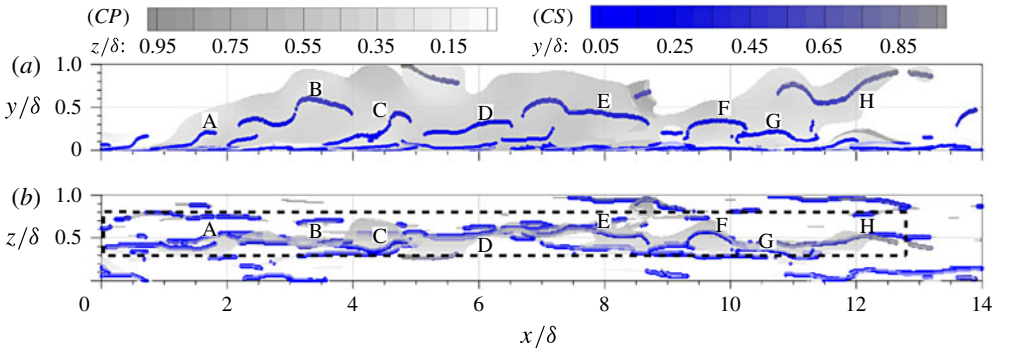

FIGURE 4. (Colour online) (*a*) Side view and (*b*) top view of a sample instantaneous flow field. The light grey isosurface and the dark grey (blue online) lines indicate *CP* and *CS*, respectively.

wall-normal outline of the low-momentum region, respectively. The streak detection proposed in the present study is applicable to the categorization of the *u*-structures by the streamwise length, and the identification of active motions by the Reynolds shear stress.

3. Population trends of negative-*u* structures

Several researchers have addressed the distributions of large-scale structures (Adrian *et al.* 2000; Ganapathisubramani *et al.* 2003; Tomkins & Adrian 2003; Dennis & Nickels 2011*b*; Baltzer *et al.* 2013); however, very-large-scale structures and the properties of several features of experimental 3D turbulence data remain to be explored. The spatial dimension of LSM and VLSM and spatial association of LSMs in a VLSM were estimated in the instantaneous flow field by using the *CS* cores, shown in figure 4. The side view of the sample snapshot (figure 4*a*) shows that eight LSMs marked 'A' to 'H' (longer than 1δ) were associated with form a very-long structure (approximately 12δ). Several low-y ($y \lesssim 0.05\delta$) streaks were positioned inside the VLSM. The top view shown in figure 4(*b*) reveals that the eight LSMs were quasi-streamwise aligned along the very-long *CP* of the low-speed structure. To shed light on size-dependent turbulent structures from a LSM and to a VLSM, this subsection provides a detailed description of the statistics of the spatial extents and the spatial association of the structures.

3.1. *Population trends of LSMs*

The population trends of LSMs were computed as a function of the streamwise length of the cores (L_{CS}) and the inclination angle of the cores (α_{CS}). Here, note that the *CS* cores longer than 1δ have been considered as LSMs, which is the same length criteria for LSMs in related studies (Dennis & Nickels 2011*a*,*b*; Baltzer *et al.* 2013). The population of *CS* cores, N_{CS}, was defined as the ensemble-averaged number of the *CS* core. According to the streamwise length and the inclination angle, the population trends were specified by $N_{CS}(L_{CS}, y)$ and N_{CS} (α_{CS}, y), respectively. The wall-normal position y of the *CS* core is determined by the most upstream position of each *CS* core (see the inset of figure 5*a*).

Figure 5(*a*) shows the averaged population of the streamwise length distribution of the *CS* core (L_{CS}) over the wall-normal position, given by $\sum_y N_{CS}(L_{CS}, y)\Delta y/\delta$.

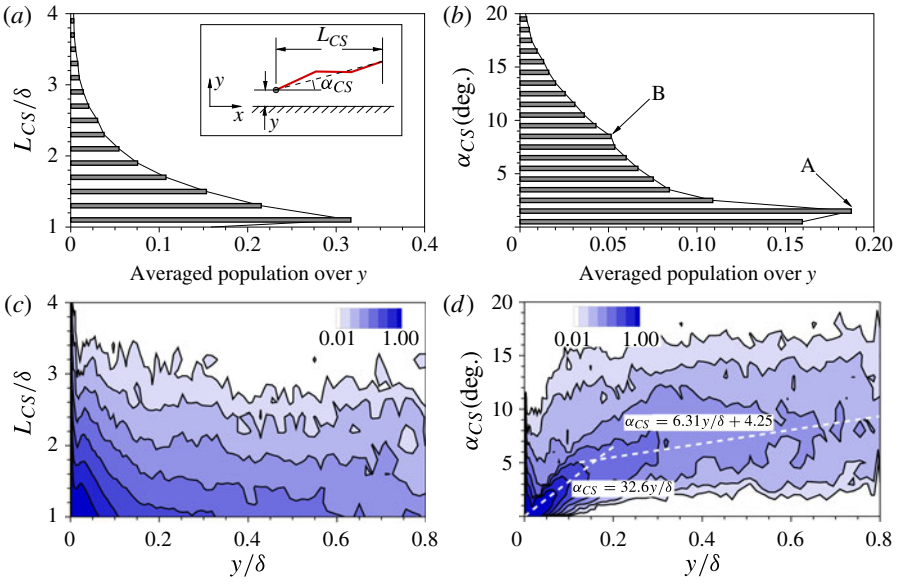

FIGURE 5. (Colour online) Population of the *CS* cores as a function of (*a*,*c*) the streamwise length with a bin size of 0.2δ and (*b*,*d*) the inclination angle with a bin size of 1°. (*a*,*b*) Averaged population over the wall-normal position. (*c*,*d*) Wall-normal distribution of the population based on the furthest upstream position (the inset of *a*). The contour level 1 means that the averaged population of *CS* core is unity in the whole wall-parallel domain ($10\pi\delta \times 3\pi\delta$).

The distribution exponentially decreases with increasing L_{CS}. The critical length of the upper limit of the LSM was 3δ in many previous studies (Guala *et al.* 2006; Balakumar & Adrian 2007; Dennis & Nickels 2011*b*). Most of the LSM streamwise lengths are less than 3δ, in particular 97.3 % of the total numbers of LSMs. Figure 5(*b*) shows the distribution of the inclination angle of the cores (α_{CS}), given by $\sum_y N_{CS}(\alpha_{CS}, y)\Delta y/\delta$. One dominant peak is seen at 1.5° (marked 'A') and one small bump at 8.5° (marked 'B'). This implies that two modes are present in the inclination angle. It is known that the shape of the LSM is dependent on the wall-normal position (Adrian *et al.* 2000).

Figure 5(*c*) shows the spatial extents of the *CS* cores as a function of the wall-normal position $N_{CS}(L_{CS}, y)$. The population at $y \approx 0$ represented the population of the wall-attached core. As shown in figure 5(*a*), the population decreased as the streamwise length (L_{CS}) and the wall-normal position y increased. Unlike the populations of the long structures ($\sim 2\delta$), the populations of the short structures ($\sim 1\delta$) rapidly decreased as the wall-normal position increased. Similarly, the high population of short structures in the near-wall region resulted from the presence of near-wall streaks (low-y *CS* cores of figures 2*d* and 4). The significant reduction in the population of short structures in the outer region facilitated the identification of long structures among the wall-detached structures as distinct from the wall-attached structures. The distribution of the inclination angles relative to the wall as a function of the wall-normal position N_{CS} (α_{CS}, y) is shown in figure 5(*d*). Because the *CS* consists of both near-wall streaks and LSMs in the outer layer, a highest density of the angle at $y \approx 0$ was observed between zero and 6°. The most populated angle increased

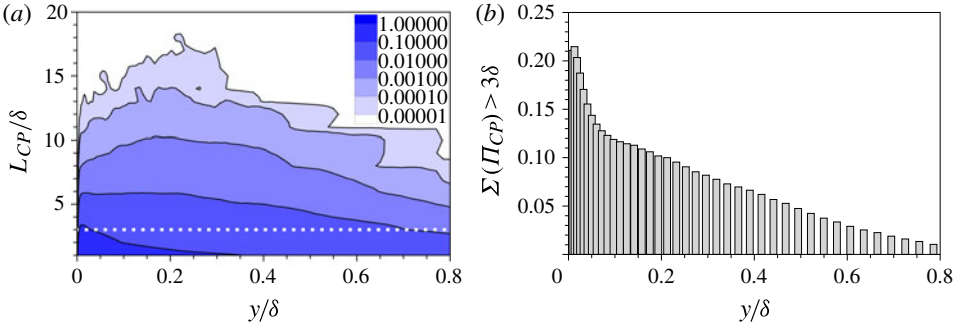

FIGURE 6. (Colour online) (*a*) The population density of the low-speed streak in the xz plane (Π_{CP}). (*b*) The cumulative density of the low-speed streak characterized by a length exceeding 3δ. Both plots were normalized by the normalized by the unit xz area ($\delta \times \delta$).

with y, in agreement with the mean growth angle of the hairpin packet (Adrian *et al.* 2000). The rate of increase steepened ($32.6°/\delta$) near the wall (wall-attached structure), whereas this rate was slow ($6.31°/\delta$) in the core region (wall-detached structure). The inclination angle ranged from 5 to 10° in the core region, with 8° being the most common value. Because the angle of *CS* core is almost half of the angle of spanwise vortices (see lines 'B' and 'C' in figure 3), this observation is in qualitatively good agreement with Adrian *et al.* (2000). Moreover, almost 14 % of the total LSMs that originated from the position $y^+ = 3.17$, spanned the region from the near-wall to the outer region ($y^+ > 50$). The wall-attached structures that stretched from the near-wall to the outer region formed bridgeheads for communicating information between the near-wall and outer regions. We tentatively supposed that the inclined LSMs attached to the wall contributed to the near-wall modulation of the small-scale structures, consistent with the previous result reported by Mathis *et al.* (2009).

3.2. *Population trends of VLSMs*

Figure 6(*a*) displays the population density of the streamwise length of the *CP* plane (Π_{CP}) in the wall-parallel plane. The population density was obtained from the number of the *CP* planes per unit area, $\Pi_{CP} = N_{CP}/L_xL_z$. The population density was high for short structures, similar to the properties of the *CS* length distribution. As the wall-normal distance increased, the density across all L_{CP} ranges decreased. The longest structure, which corresponded to the longest cross-sectional length in the wall-parallel plane, decreased along the wall-normal distance from the wall. The shapes of the VLSMs were conjectured to be wide roots attached to the wall with multiple stems that represented ramp-shaped hairpin packets (Kim & Adrian 1999). Thus, the longest L_{CP} decreased in the outer region. Very long structures up to 18δ in length were observed, although their density was low. A threshold of zero resulted in the detection of very long structures up to 26δ in length near the top of the log layer (see § A.2). Although the population density of the very-long structures was affected by the choice of threshold, the behaviour of the population trend was not significantly influenced, except for the maximum streamwise extent of the VLSMs (Baltzer *et al.* 2013). The densities of the 3δ- and 5δ-long structures were 0.0448 and 0.0159, respectively, at $y = 0.15\delta$, indicating the presence of approximately 14 and 5 long structures, respectively, within the whole computational domain. The

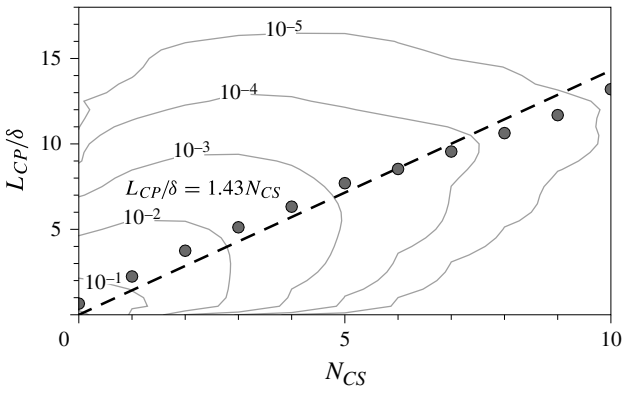

FIGURE 7. JPDF of the streamwise length of the CP cores (L_{CP}) and the number of long ($>1\delta$) *CS* cores (N_{CS}). The contour levels are from 10^{-5} to 10^{-1}. The bin sizes are 0.5δ and 1 for N_{CP} and N_{CS}, respectively. The symbols indicate the expectation of L_{CP} at each N_{CS}, $E[L_{CP}]$.

exponentially decaying statistics agreed qualitatively with the results obtained by Dennis & Nickels (2011*b*). For the cumulative population density for $L_{CP}/\delta > 3$, $\sum_{L_{CP}=3\delta}^{\infty} \Pi_{CP}(L_{CP}, y) = 0.111$ at $y = 0.15\delta$ (figure 6*b*), which corresponds to 33 very long structures ($>3\delta$) in the log layer over the whole domain. The present result confirms that the observation of a very-long structure ($>3\delta$) is very common.

3.3. *Spatial association of LSM and VLSM*

In order to see the relationship between the numbers of LSMs in a VLSM, the joint probability density function (jpdf) of L_{CP} and N_{CS} is shown in figure 7. Note that the long *CS* cores longer than 1δ in the streamwise direction were sampled in order to count the numbers of the LSMs. Because the *CS* cores involve both near-wall streaks and outer LSMs, the *CS* cores which reside in the viscous wall region ($y^+ < 50$) were neglected to exclude the near-wall streaks. The expectation of the streamwise length of *CP* is denoted by a symbol defined by

$$E[L_{CP}](N_{CS}) = \frac{\sum_l (L_{CP}\ \mathrm{jpdf}(L_{CP}, N_{CS}))_l}{\sum_l (\mathrm{jpdf}(L_{CP}, N_{CS}))_l}, \tag{3.1}$$

where l is an index of N_{CS}-bin. Owing to the very strict condition in length and height for the effective outer LSMs, we observed a wide variation of the *CP* length at $N_{CS} = 0$. The expectation (symbol) showed a roughly linear relationship between the number of LSMs and the streamwise lengths of the *CP* cores, i.e. $L_{CP}/\delta = 1.43N_{CS}$. This relation is qualitatively in good agreement with the observation in figure 4, e.g. 8 LSMs in a 12δ-long VLSM. When the VLSM is defined as a structure having multiple outer LSMs ($N_{CS} \geqslant 2$), the critical length between LSM and VLSM is approximately 2.9δ from the linear relation. This critical length is very close to the previous critical length 3δ (Guala *et al.* 2006; Balakumar & Adrian 2007; Dennis & Nickels 2011*b*). The lengths of the VLSMs increased with the number of LSMs, supporting the hypothesis based on the concatenation concept (Kim & Adrian 1999; Guala *et al.* 2006; Baltzer *et al.* 2013). The VLSM formation mechanism was clarified by assessing the temporal information obtained from the streamwise-aligned LSMs.

The number of LSMs in a VLSM was previously estimated by the number of bulges present (Guala *et al.* 2006; Lee & Sung 2011; Baltzer *et al.* 2013). The present work offers a different set of measures that may be used to characterize the presence and position of an LSM in a VLSM.

4. Time-evolution of the LSMs and VLSMs

The previous section showed that a VLSM consists of multiple LSMs along the streamwise direction. The temporal characteristics of the LSMs during the formation of the VLSMs were investigated by tracking the LSMs and VLSMs.

4.1. *Upstream tracking of LSMs and VLSMs*

We first traced the long and very-long negative-u streaks in the wall-parallel cross-section. The time variance of the structures could be categorized into seven events:

(*a*) *preserving*, if the number of streaks and the lengths of the streaks were preserved (the changes in these values did not exceed Δx_{subdom} ($\Delta x^+_{subdom} = 23.4$));
(*b*) *merging*, if several streaks present in the previous step formed a single long streak;
(*c*) *breaking*, if a long streak present in the previous step fractured in the present step;
(*d*) *growing*, if a short streak present in the previous step lengthened;
(*e*) *shortening*, if a long streak present in the previous step shortened;
(*f*) *creating*, if a streak in the present step were newly formed without relationship to streaks present in the previous step;
(*g*) *extincting*, if a streak in the previous step disappeared in the present step.

Here, the streaks in the upstream ($x_{ref} - U_c \Delta t_{track}$; U_c is the convection velocity) of the previous time step ($t_{ref} - \Delta t_{track}$) are traced by the reference position (x_{ref}) of the present time step (t_{ref}), i.e. upstream tracking, and the extinction event could be ignored. The merging and breaking, growing and shortening, and creating and extincting event pairs were central to describing the scale of the time-dependent changes.

Figure 8 shows a sample time series of images of the streaks based on L_{CP} at $y = 0.15\delta$. White lines indicate positions of $CP = -1$. As shown, all events occurred simultaneously. For example, two streaks became a single long streak through a merging event (marked 'A') in which the gap distance of 0.2δ was closed for $4\delta/U_{CL}$. The growing event (marked 'D') shows that the structures increased in size from 1.2δ to 1.4δ for $4\delta/U_{CL}$. The shortening event (marked 'E') corresponded to a reduction in the structure size from 0.9δ to 0.8δ for $4\delta/U_{CL}$. The observations obtained from the instantaneous evaluation could not be generalized because the evaluation was carried out within the sampled period. By tracking all streaks at each snapshot, the six event categories could be employed to characterize the temporal changes in the streaks. Figure 9(*a*,*b*) show the conditional population densities of the LSMs ($\Pi_{CP}|1\delta \leqslant L_{CP} < 3\delta$) and VLSMs ($\Pi_{CP}|L_{CP} \geqslant 3\delta$), respectively. Here, LSMs longer than 1δ were traced in the former snapshot in time intervals $\Delta t_{track} = 0.1\delta/U_{CL}$ (or $\Delta t^+_{track} = 3.09$) to examine the formation mechanism of LSMs and VLSMs. Note that the conditional population densities are insensitive to the time interval up to $\Delta t_{track} = 0.3\delta/U_{CL}$ (not shown). Streaks characterized by $1\delta \leqslant L_{CP} < 3\delta$ were dominated by merging, growing and shortening events. Although the frequency of merging

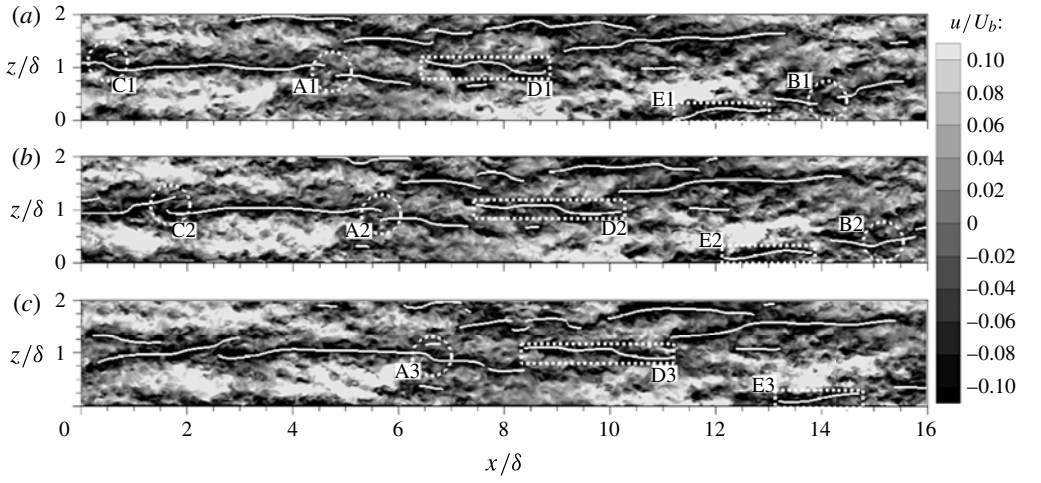

FIGURE 8. Instantaneous flow fields in the wall-parallel plane at $y = 0.15\delta$: (*a*) $t = t_{ref} - 4\delta/U_{CL}$, (*b*) $t = t_{ref} - 2\delta/U_{CL}$ and (*c*) $t = t_{ref}$ ($t_{ref} = 360\delta/U_{CL}$). The marks 'A' and 'B' indicate a merging event; mark 'C' indicates a breaking event; mark 'D' indicates a growing event in a single streak; mark 'E' indicates a shortening event in a single streak.

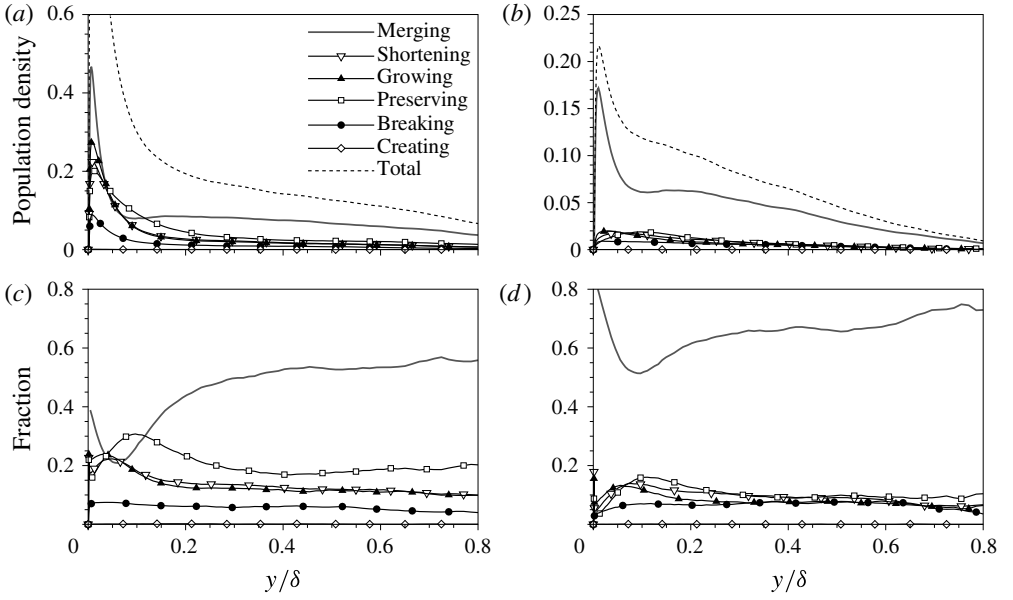

FIGURE 9. (*a*,*b*) The population density and (*c*,*d*) fraction of the negative-u structures, classified in terms of the time evolution of the structures, for (*a*,*c*) $1\delta \leqslant L_{CP} < 3\delta$ and (*b*,*d*) $L_{CP} \geqslant 3\delta$ at $\Delta t_{track} = 0.1\delta/U_{CL}$ ($\Delta t^{+}_{track} = 3.09$): (*a*) $1\delta \leqslant L_{CP} < 3\delta$; (*b*) $L_{CP} \geqslant 3\delta$; (*c*) $1\delta \leqslant L_{CP} < 3\delta$; (*d*) $L_{CP} \geqslant 3\delta$.

event was dominant in the outer region, the frequencies of growing and shortening events were similar to that of merging event in the region $0.05\delta < y < 0.1\delta$. The populations of the growing and shortening events were nearly identical. These events

corresponded to changes in the spatial dimensions of the features with preservation of the overall population of streaks (multiple streaks did not interact). Although growing and shortening events were comparably frequent, the spatial dimensions tended to increase by 2 % per unit time and decrease by 1 % per unit time, on average (data not shown). Thus, the scale of the LSMs tended to increase overall over the duration of the measurement. The population density revealed that the scale decrease caused by breaking events contributed only a small degree in the outer region. The merging processes increased the overall scale of the LSMs in the outer region, although the number of LSM merging processes decreased with time. Small-scale seed structures were generated during creating events, and these events were mainly associated with regions characterized by $L_{CP} < 1\delta$. Thus, a large number of low-speed regions ($1\delta \leqslant L_{CP} < 3\delta$) with lengths that were comparable to or larger than the average LSM length arose from the growth and merging of small-scale streamwise extents. This statistical study showed that the dominant mechanism by which the 1δ- to 3δ-long streaks were retained relied on growing and merging events.

The distribution of events was substantially different among the 3δ-over structures. Structures characterized by $L_{CP} \geqslant 3\delta$ (figure 9*b*) were more highly dominated by merging events than were structures characterized by $1\delta \leqslant L_{CP} < 3\delta$ (see figure 9*b*,*d*). The population density of the preserving events decreased to a lesser extent than that was observed among the large-scale structures ($1\delta \leqslant L_{CP} < 3\delta$). This observation may have arisen from the ratio $\Delta x_{subdom}/L_{CP}$, which indicates the smallest unit for detecting the change. The shortening and growing events contributed similarly to the statistics, and their populations were smaller than the population of merging event in all y positions. The population of breaking events decreased as L_{CP} increased. The VLSM breaking events occurred after structures longer than 3δ had formed. Although the time-varying characteristics of the LSMs and VLSMs differed significantly in the low-speed region, the merging event dominated both the LSMs and VLSMs. Most VLSMs formed as a result of merging events among the short and long structures. The VLSMs were finally dispersed or broken after splitting into structures shorter than the L_{CP} range. As a result, the total area of the low-speed region remained constant over time. Although the merging event was significant for the creation of VLSMs, it was not clear which mechanism were involved in the formation of the VLSM. Statistical evidence supporting the velocity fields around the merging events was examined, as discussed in the following section.

4.2. *Formation of VLSMs – a detailed analysis of the merging events*

Lee & Sung (2011) reported that VLSMs formed by merging processes occur when the upstream head (UH; the most downstream position of the upstream structure) and the downstream tail (DT; the most upstream position of the downstream structure) are proximal. Figure 10 shows that visualizing the instantaneous flow fields prior to a merging event provide a general understanding of this process. Note that labels A1, A2 and A3 are the same as in figure 8. This figure illustrates the merging of two LSMs in an outer region (light grey isosurface). Although the near-wall streaks (dark grey isosurface) were already connected prior to $t_{merging}$, the merging among the outer structures occurred afterward. Because the merging event occurred by closing the gap distance between two LSMs, we suppose the origin of the merging event herein by the difference between the convection velocities in the UH and DT. This hypothesis was tested by estimating the local convection velocities at the DT and the UH, as shown in figure 11. The local convection velocity was conditionally sampled at the head and tail

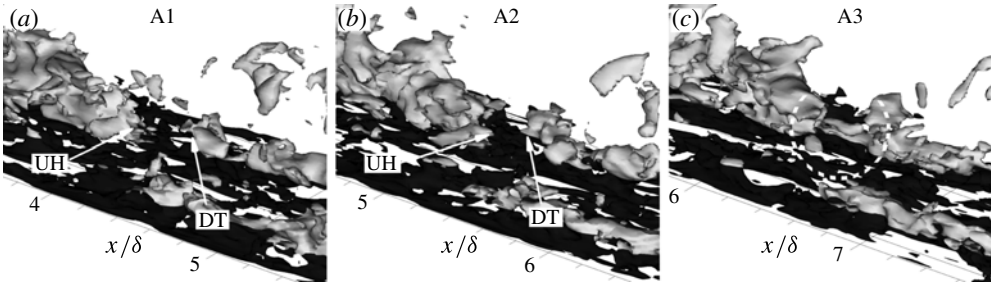

FIGURE 10. Isosurfaces of the streamwise velocity fluctuations ($u = -0.1U_b$) at (*a*) $t = t_{merging} - 4\delta/U_{CL}$, A1; (*b*) $t = t_{merging} - 2\delta/U_{CL}$, A2; and (*c*) $t = t_{merging}$ ($t_{ref} = 360\delta/U_{CL}$), A3. In (*a–c*), dark and light grey indicate $y < 0.15\delta$ and $y \geqslant 0.15\delta$, respectively.

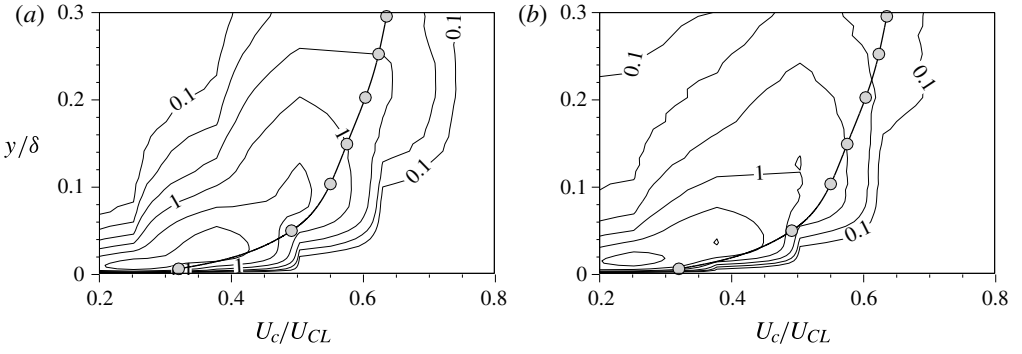

FIGURE 11. Distributions of the convection velocity (U_c) at (*a*) the UH and (*b*) the DT. In (*a*,*b*), the conventional convection velocity is denoted by a symbol. Contour levels are shown in seven levels from 0.1 to 10 (exponential distribution).

positions. For $\Delta t_{track} = 0.2\delta/U_{CL}$ ($\Delta t^+_{track} = 6.18$), prior to merging, the local convection velocity was obtained from the convection distance, which was evaluated from the relative distance between the maximum values of the autocorrelation function. The conventional convection velocity was obtained from the spatiotemporal correlations of the streamwise velocity fluctuations, for comparison (Kim & Hussain 1993). Figure 11 shows that the most distributed convection velocities of both the UH and DT were lower than the conventional convection velocity due to a focus on the low-momentum regions. The convection velocity of the UH was higher than that of the DT. This result indicated that the UH moved faster than the DT.

The distribution of convection velocities revealed that the convection velocities of the UH and DT were locally different, even at a given wall-normal distance. We next examined the conditionally sampled convection velocity to investigate the possible reasons underlying this velocity difference. Figure 12 shows the spatiotemporal correlation, $R[A, B](r, \Delta t) = \langle A(x, t)B(x + r_x, t + r_t)\rangle$, between the positive-$u$ (u_{pos}) and negative-u (u_{neg}) velocities, which was used to obtain the conditionally sampled convection velocity. Here u_{pos} and u_{neg} were defined as

$$u_{pos} = \begin{cases} u & \text{if } u > 0 \\ 0 & \text{otherwise} \end{cases} \quad \text{and} \quad u_{neg} = \begin{cases} u & \text{if } u < 0 \\ 0 & \text{otherwise.} \end{cases} \tag{3.2a,b}$$

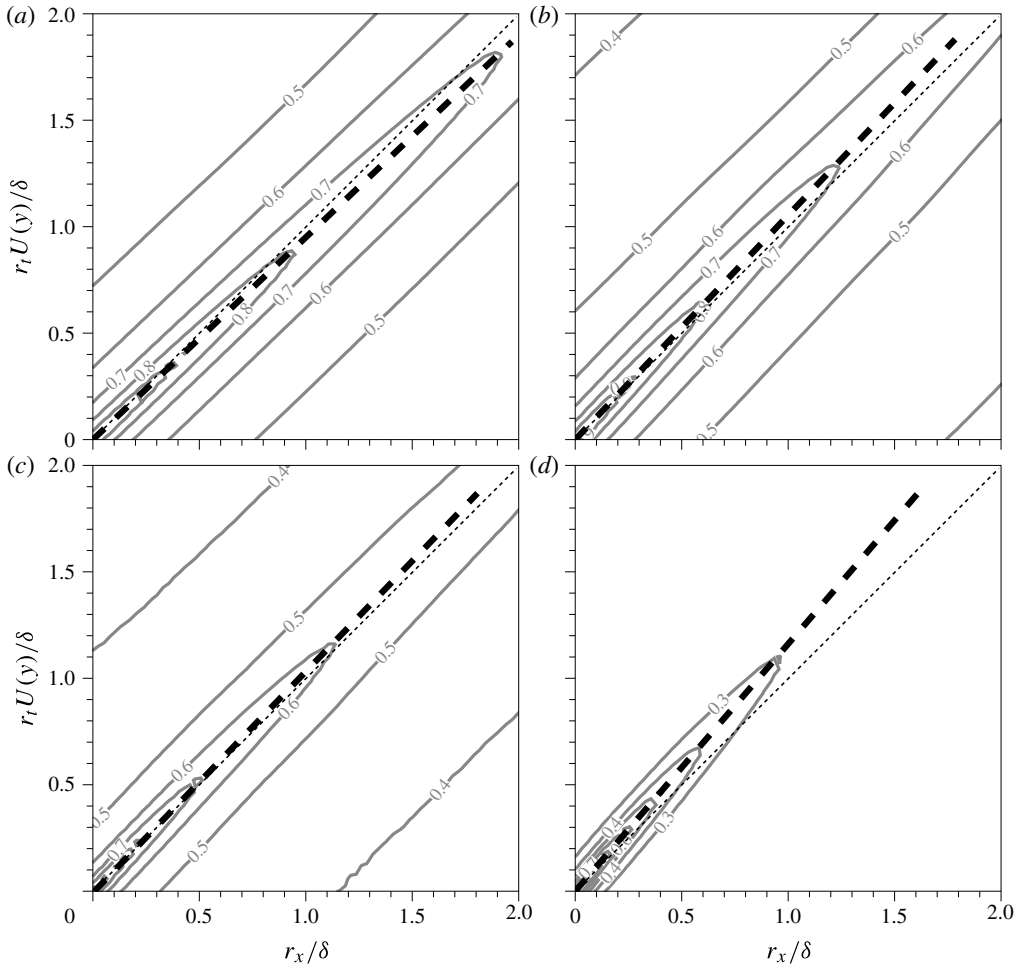

FIGURE 12. Spatiotemporal correlations of the streamwise velocity fluctuations at $y/\delta = 0.15$: (*a*) the positive-u correlation ($u > 0$), (*b*) the negative-u correlation ($u < 0$), (*c*) the strong negative-u correlation ($u \leqslant -0.1U_b$), (*d*) the weak negative-u correlation ($-0.1U_b < u \leqslant 0$).

The line contours were denoted $R[u_{pos}, u_{pos}]$ and $R[u_{neg}, u_{neg}]$ in figure 12(*a*,*b*), respectively, and were normalized by the correlation at the reference position and time. The angle of the symmetric line of the low-speed region (dashed line in figure 12*b*) exceeded that of the high-speed region (dashed line in figure 12*a*). Because the vertical axis was multiplied by the mean streamwise velocity $U(y)$, the convection velocity was the same as $U(y)$ when the slope of the symmetric line was unity (dotted line). As expected, the convection velocity of the low-speed region was lower than the mean streamwise velocity, and the velocity in the high-speed region exceeded the mean streamwise velocity. The slow convection in the low-speed LSMs was consistent with the results reported by Chung & McKeon (2010). Further to the findings discussed above, figure 12(*c*,*d*) show the influence of the magnitude of u on the convection velocity. The negative velocity fluctuations could be divided into mild

or strong fluctuations, depending on the magnitude of the fluctuations

$$u_{neg}^{mild} = \begin{cases} u & \text{if } -u_{th,raw} \leqslant u < 0 \\ 0 & \text{otherwise} \end{cases} \quad \text{and} \quad u_{neg}^{strong} = \begin{cases} u & \text{if } u < -u_{th,raw} \\ 0 & \text{otherwise.} \end{cases} \tag{3.3a,b}$$

The observation of a higher slope in the weak negative-u correlation contours, relative to the slope of the strong negative-u correlation, suggested that the weak negative-u structure convected more rapidly than the strong negative-u structure. The convection velocity depended not only on the sign of the velocity fluctuations, but also on the velocity magnitude. Although the range was divided into two ranges, the convection velocity decreased as the velocity fluctuations decreased. Although this finding appears simple, it reveals an important observation that the merging of large scales originates from the differences in the velocity fluctuations. In other words, wherever two streamwise-aligned structures with different velocity fluctuations exist, the structures are merged by the local convection velocity difference unless the low-speed region is completely balanced with adjacent high-speed regions. Unlike predictions based on the spatial dimensions of the coherent structures or a spectral analysis, the variations in the relative convection velocities may be predicted without the need for a complicated model. The present results indicate that any region characterized by large velocity fluctuation differentials can support the primary mechanism that drives merging events toward the formation of VLSMs.

The merging process was further examined by conditionally averaging the velocity fields around the DTs. As shown in figure 13, the conditional average $\langle u|CP^{DT}(y_{ref} = 0.15\delta)\rangle$ was obtained, where CP^{DT} indicates the position of the DT in the negative CP cores ($CP = -1$). The time series was obtained by conditionally averaging the velocity fields over time, relative to the merging instant. A ramp-shaped tail was present in the downstream of the merging event and a head was present in the upstream (figure 13*a*). Immediately before and after the merging event, the narrow region between the DT and UH was characterized as a mild-low-speed region, i.e. a relatively high-speed region rather than either DT or UH. The near-wall structures were unified prior to $t_{merging} - 0.8\delta/U_{CL}$ whereas the structures in the outer region merged within the time period. This time series revealed that the merging of negative-u regions in the outer region occurred over a long period of time. Variations between the weak negative-u region (white) between the two structures were dominant, whereas the strong negative-u region (black) was nearly stationary. The strong region grew smaller as the upstream structures approached the downstream structures. When the merging process is almost completed (figure 13*d*), the process becomes slow due to the small difference of velocity at the boundary. Again, this supports our model of merging events in which VLSMs are created from LSMs. The reduced volume of the strong negative-u region indicated that the energy decreased during the merging event. The present study supports that the merging of upstream large-scale structures contributed to the formation of VLSMs (Kim & Adrian 1999; Guala *et al.* 2006; Lee & Sung 2011). Apparently, the alignment of the positive- and negative-u structures (McKeon & Sharma 2010; Hellström *et al.* 2011; Sharma & McKeon 2013) may be an essential prerequisite to the formation of VLSMs in the proposed merging model.

5. Summary and conclusions

Direct numerical simulations were performed to investigate the spatial features of the large- and very-large-scale structures in a turbulent channel flow. The computational domain was set to $10\pi\delta(x) \times 2\delta(y) \times 3\pi\delta(z)$ and the friction Reynolds number Re_τ was 930. We proposed a detection algorithm for the structures based on

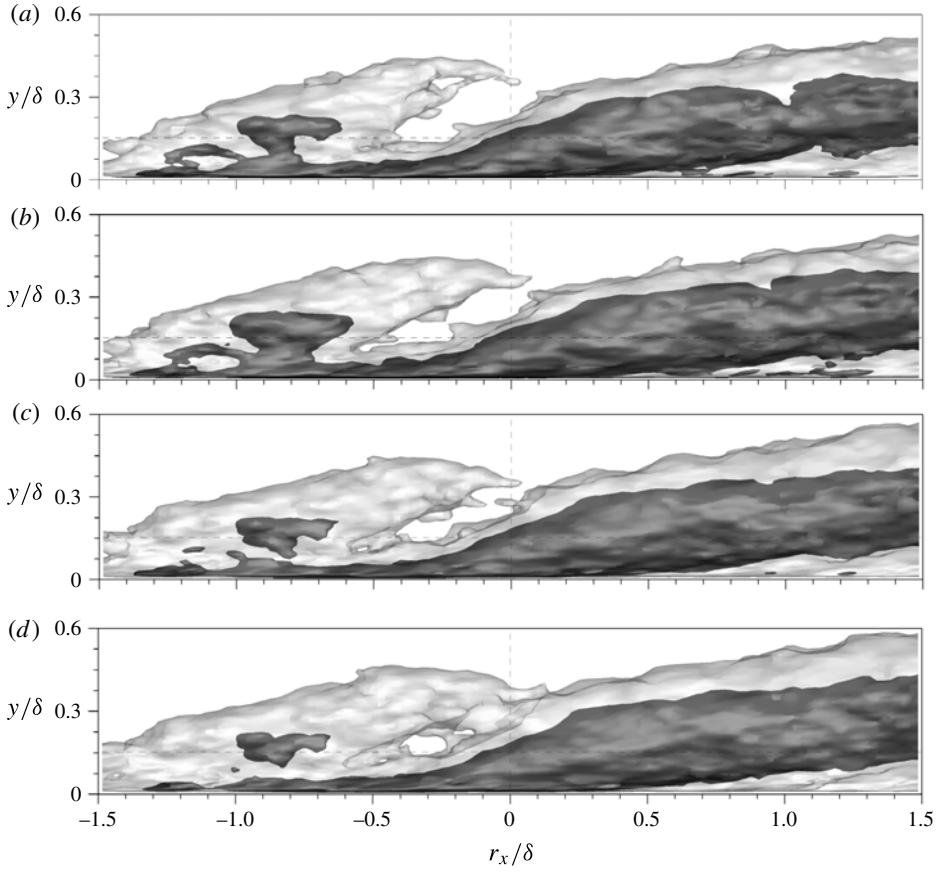

FIGURE 13. Time series of the conditionally averaged velocity fields based on the position of the downstream-tail streak at $y_{ref} = 0.15\delta$ $\langle u|CP^{DT}(y_{ref} = 0.15\delta)\rangle$: (*a*) $t = t_{merging} - 0.8\delta/U_{CL}$; (*b*) $t = t_{merging} - 0.6\delta/U_{CL}$; (*c*) $t = t_{merging} - 0.4\delta/U_{CL}$; (*d*) $t = t_{merging} - 0.2\delta/U_{CL}$. Light and dark grey isosurfaces were formed using $u = -0.0160U_b$ (45 % of the maximum value of u) and $u = -0.0213U_b$ (60 % of the maximum value of u), respectively. The black dashed lines indicate the reference positions.

the characteristic spines of LSMs and the CP of u structures. The near-wall and outer structures in instantaneous flow fields were identified by the streamwise dimension of negative-u structures. The detected outer LSMs (defined herein as 1–3δ) and VLSMs (defined herein as $>3\delta$) were traced individually to examine the spatial and temporal characteristics of the structures. The populations identified by the characteristic spines showed that a fraction of LSMs shorter than 3δ is 97.3 %. The inclination angle of a LSM increases along with increasing the wall-normal distance. Because many of wall-attached LSMs reach the outer region, the LSMs form bridgeheads for communication between the near-wall and the outer regions. The populations of VLSMs identified by the very-long CP ($>3\delta$) showed that the longest structure length was sensitive to the threshold value, which was 18δ in the present threshold. The observations of VLSMs were very common. The streamwise length of the VLSMs increased linearly with the number of outer LSMs. The negative-u structure longer than approximately 3δ was confirmed as a VLSM, in terms of multiple LSMs.

The added number of outer LSMs further supported a model in which the LSMs concatenated to form VLSMs.

Conditionally-averaged population trends by the upstream tracking showed that the dominant formation mechanism of VLSMs is the merging of LSMs, while that of LSMs is both merging and growing events. The origin of the merging event was investigated by comparing the convection velocities of the large-scale structure. The upstream (chasing) structures generally convect faster than the downstream (chased) structures. The spatiotemporal correlation of the streamwise velocity fluctuations showed that the convection velocity depends on the streamwise velocity fluctuations. This eventually led to the concatenation between in-line low-speed structures. The behaviour of in-line negative-u structures before the merging event was visualized by the conditionally averaged velocity fields. The fast convection of weak negative-u regions played a crucial role of the formation of VLSMs. While the positions of strong negative-u regions were almost stationary, the strong regions grew smaller as the upstream structures approached the downstream structures. The VLSMs are observed at where the large difference of u is present during the stabilization process. An alternative alignment of the positive- and negative-u structures was conjectured to be a precondition for the formation of VLSMs.

Acknowledgements

This work was supported by the Creative Research Initiatives program (No. 2014-001493) of the National Research Foundation of Korea (MSIP) and partially supported by the Supercomputing Center (KISTI).

Supplementary movies

Supplementary movies are available at http://dx.doi.org/10.1017/jfm.2014.249.

Appendix A. Additional description of the detection method

The present study introduced a modified method for detecting negative-u structures. To reduce small-scale motions, a 2D Gaussian filter and a long-pass filter were applied in the cross-stream plane and in the streamwise direction, respectively. Here, the standard deviation $\sigma(y)$ represents the strength of the Gaussian filter. The regions of velocity fluctuations in the filtered field that were stronger than a threshold value were identified as an effective structure. Thus, the threshold value u_{th} affected the results (Baltzer *et al.* 2013). The cutoff wavelength used to distinguish between large and very large structures is usually 1δ (Mathis *et al.* 2009). The dependence of the detection results on $\sigma(y)$ and u_{th} were examined.

A.1. *Influence of* $\sigma(y)$

Figure 14 shows the filtered fields and the detected *CS* cores with respect to the standard deviation. In the present study, the standard deviation $\sigma(y)$ was determined based on the average spanwise dimensions of the streaky structures. Because the $\sigma(y)$ value was determined from the first crossing of $R_{uu} = 0.5$ (see (2.3)), $\sigma(y)$ varied from 0.0202 (at $y^+ = 6$) to 0.170 (at $y = 0.7\delta$). Unlike $\sigma(y)$ (figure 14*a*), the constant standard deviation σ reflected the spatial characteristics at a certain wall-normal position. For instance, the values of $\sigma = 0.15$ in figure 14(*b*) and $\sigma = 0.05$ in figure 14(*c*) represent the spanwise half-width of $R_{uu} = 0.5$ at $y = 0.436\delta$ and $y = 0.0698\delta$ ($y^+ = 64.9$), respectively. Thus, the large standard deviation reduced the number of near-wall structures (both *CS* and *CP* in figure 14*b*). By contrast, a smaller standard deviation resulted in the introduction of many strong small-scale

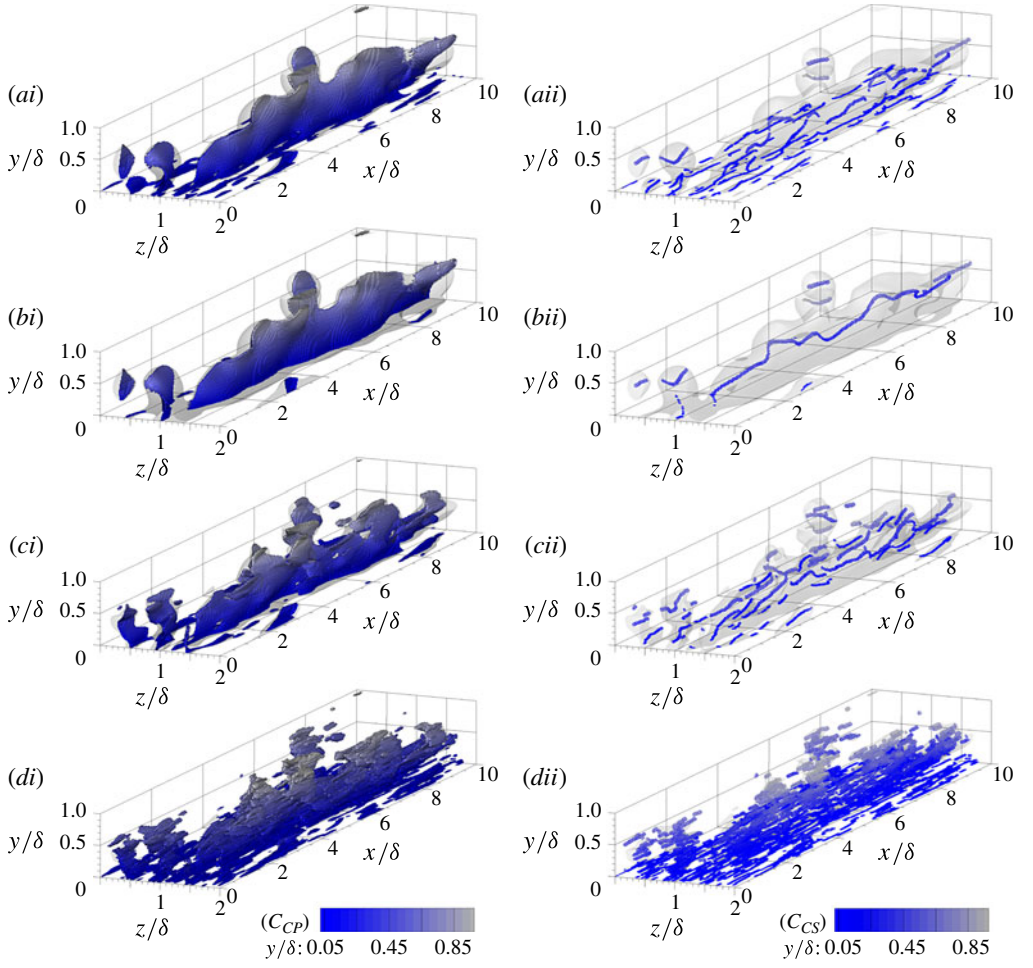

FIGURE 14. (Colour online) Isosurfaces of the local extrema of the negative-u: (*i*) in the z direction (*CP*); (*ii*) in the streamwise plane (*CS*). All figures contain the filtered flow field $\hat{u}$ ($=-u_{th}$; transparent grey). Two-dimensional Gaussian filter, with standard deviations of (*a*) $\sigma(y/\delta)$ from (2.3), (*b*) $\sigma(y/\delta)=0.15$ and (*c*) $\sigma(y/\delta)=0.05$. (*d*) Filtered field obtained without the application of the 2D Gaussian filter.

motions in the outer region that led to a large number of discontinuous *CS* cores and *CP* planes (figure 14*c*). If the 2D Gaussian filter was not applied prior to the streak detection process (figure 14*d*), the detected cores consisted of totally discontinuous lines inside a single negative-u structure. Because strong u-fluctuations in the raw velocity field contained both near-wall and outer structures in figure 14(*ai*), the standard deviation as a function of y was calculated to facilitate a representation of the structures across the entire domain. The inclined nature of the *CS* core was observed in both $\sigma(y)$ and the constant σ. The fragments of the *CS* core at small constant values of σ (figure 14*ci*) resembled the continuous *CS* core in the $\sigma(y)$ (figure 15*ai*). Although $\sigma(y)$ was applied, the detected core, which spanned the vertical direction, represented an inclined structure.

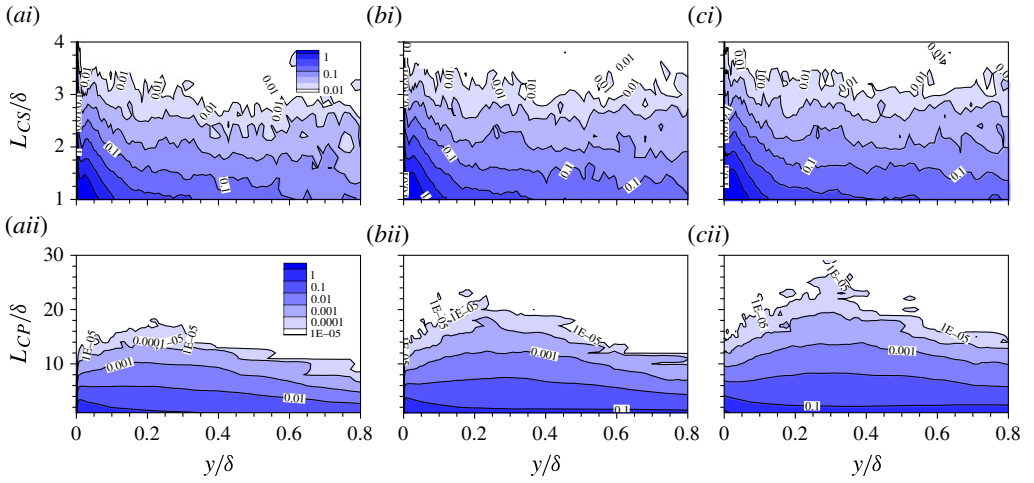

FIGURE 15. (Colour online) Two-dimensional histogram of the population of the streamwise length. The threshold values were (*a*) $u_{th,raw} = 0.1U_b$, (*b*) $u_{th,raw} = 0.05U_b$ and (*c*) $u_{th,raw} = 0$, where U_b is the bulk velocity. The population of (*i*) L_{CS} represents the streamwise length of the packet-like structures (*CS*) and (*ii*) L_{CP} represents the streamwise length of the cross-section of the negative-u region in the wall-parallel plane (*CP*). The population of L_{CP} was normalized by the wall-parallel area.

A.2. *Influence of* u_{th}

Figure 15 depicts the population densities of both L_{CS} and L_{CP}, which indicate the streamwise lengths of the *CS* cores and *CP* planes, respectively. The influence of u_{th} on the population density was explored based on three different threshold values: $u_{th} = 0.1U_b$, $0.05U_b$ and zero. Note that the same spatial filtering was used in all cases, as shown in § 2.2. The region recognized as an effective structure was found to extend as u_{th} decreased. Weak turbulent motions that were not visible upon application of the larger threshold were recognized as effective structures upon application of the smaller threshold. In short, the total number of detected structures and the maximum lengths of the structures increased as u_{th} decreased. Although the population trend depended on u_{th}, the overall population trend did not change significantly with u_{th} (Dennis & Nickels 2011*b*; Baltzer *et al.* 2013); however, the population of the longest structure decreased significantly for larger u_{th} (see figure 15*aii*,*cii*), in agreement with Baltzer *et al.* (2013). For example, the longest structure of *CP* was 26δ for the zero threshold (figure 15*cii*), whereas this value was 18δ for a threshold of 10 % of the bulk velocity (figure 15*aii*). The relatively large threshold used in the present study provided a population trend that reliably described the very long structures ($>3\delta$).

REFERENCES

ADRIAN, R. J., MEINHART, C. D. & TOMKINS, C. D. 2000 Vortex organization in the outer region of the turbulent boundary layer. *J. Fluid Mech.* **422**, 1–54.

BAILEY, S. C., KUNKEL, G. J., HULTMARK, M., VALLIKIVI, M., HILL, J. P., MEYER, K. A., TSAY, C., ARNOLD, C. B. & SMITS, A. J. 2010 Turbulence measurements using a nanoscale thermal anemometry probe. *J. Fluid Mech.* **663**, 160–179.

BALAKUMAR, B. J. & ADRIAN, R. J. 2007 Large- and very-large-scale motions in channel and boundary-layer flows. *Phil. Trans. R. Soc. Lond.* A **365**, 665–681.

BALTZER, J. R., ADRIAN, R. J. & WU, X. 2013 Structural organization of large and very large scales in turbulent pipe flow simulation. *J. Fluid Mech.* **720**, 236–279.

BUSCHMANN, M. H. & GAD-EL-HAK, M. 2010 Normal and cross-flow Reynolds stresses: differences between confined and semi-confined flows. *Exp. Fluids* **49**, 213–223.

CHRISTENSEN, K. T. & ADRIAN, R. J. 2001 Statistical evidence of hairpin vortex packets in wall turbulence. *J. Fluid Mech.* **431**, 433–443.

CHUNG, D. & MCKEON, B. J. 2010 Large-eddy simulation of large-scale structures in long channel flow. *J. Fluid Mech.* **661**, 341–364.

DEL ÁLAMO, J. C., JIMÉNEZ, J., ZANDONADE, P. & MOSER, R. D. 2004 Scaling of the energy spectra of turbulent channels. *J. Fluid Mech.* **500**, 135–144.

DEL ÁLAMO, J. C., JIMÉNEZ, J., ZANDONADE, P. & MOSER, R. D. 2006 Self-similar vortex clusters in the turbulent logarithmic region. *J. Fluid Mech.* **561**, 329–358.

DENNIS, D. J. C. & NICKELS, T. B. 2008 On the limitations of Taylor's hypothesis in constructing long structures in a turbulent boundary layer. *J. Fluid Mech.* **614**, 197–206.

DENNIS, D. J. C. & NICKELS, T. B. 2011*a* Experimental measurement of large-scale three-dimensional structures in a turbulent boundary layer. Part 1. Vortex packets. *J. Fluid Mech.* **673**, 180–217.

DENNIS, D. J. C. & NICKELS, T. B. 2011*b* Experimental measurement of large-scale three-dimensional structures in a turbulent boundary layer. Part 2. Long structures. *J. Fluid Mech.* **673**, 218–244.

DUGGLEBY, A., BALL, K. S. & SCHWAENEN, M. 2009 Structure and dynamics of low Reynolds number turbulent pipe flow. *Phil. Trans. R. Soc.* A **367**, 473–488.

ELSINGA, G. E., POELMA, C., SCHRÖDER, A., GEISLER, R., SCARANO, F. & WESTERWEEL, J. 2012 Tracking of vortices in a turbulent boundary layer. *J. Fluid Mech.* **697**, 273–295.

GANAPATHISUBRAMANI, B., LONGMIRE, E. K. & MARUSIC, I. 2003 Characteristics of vortex packets in turbulent boundary layers. *J. Fluid Mech.* **478**, 35–46.

GUALA, M., HOMMEMA, S. E. & ADRIAN, R. J. 2006 Large-scale and very-large-scale motions in turbulent pipe flow. *J. Fluid Mech.* **554**, 521–542.

HELLSTRÖM, L. H. O., SINHA, A. & SMITS, A. J. 2011 Visualizing the very-large-scale motions in turbulent pipe flow. *Phys. Fluids* **23**, 011703.

HOYAS, S. & JIMÉNEZ, J. 2006 Scaling of the velocity fluctuations in turbulent channels up to $Re_{tau} = 2003$. *Phys. Fluids* **18**, 011702.

HULTMARK, M., VALLIKIVI, M., BAILEY, S. C. C. & SMITS, A. J. 2012 Turbulent pipe flow at extreme Reynolds numbers. *Phys. Rev. Lett.* **108**, 094501.

HUTCHINS, N. & MARUSIC, I. 2007 Evidence of very long meandering features in the logarithmic region of turbulent boundary layers. *J. Fluid Mech.* **579**, 1–28.

JEONG, J. & HUSSAIN, F. 1995 On the identification of a vortex. *J. Fluid Mech.* **285**, 69–94.

KIM, J. 2012 Progress in pipe and channel flow turbulence, 1961–2011. *J. Turbul.* **13** (45), 1–19.

KIM, K. C. & ADRIAN, R. J. 1999 Very large-scale motion in the outer layer. *Phys. Fluids* **11**, 417–422.

KIM, K., BAEK, S. J. & SUNG, H. J. 2002 An implicit velocity decoupling procedure for the incompressible Navier–Stokes equations. *Intl J. Numer. Meth. Fluids* **38**, 125–138.

KIM, J. & HUSSAIN, F. 1993 Propagation velocity of perturbations in turbulent channel flow. *Phys. Fluids* **5**, 695–706.

LEE, J., JUNG, S. Y., SUNG, H. J. & ZAKI, T. A. 2013 Effect of wall heating on turbulent boundary layers with temperature-dependent viscosity. *J. Fluid Mech.* **726**, 196–225.

LEE, J.-H. & SUNG, H. J. 2009 Structures in turbulent boundary layers subjected to adverse pressure gradients. *J. Fluid Mech.* **639**, 101–131.

LEE, J. H. & SUNG, H. J. 2011 Very-large-scale motions in a turbulent boundary layer. *J. Fluid Mech.* **673**, 80–120.

LEE, J. H. & SUNG, H. J. 2013 Comparison of very-large-scale motions of turbulent pipe and boundary layer simulations. *Phys. Fluids* **25**, 045103.

MARUSIC, I., MATHIS, R. & HUTCHINS, N. 2010 High Reynolds number effects in wall turbulence. *Intl J. Heat Fluid Flow* **31**, 418–428.

MATHIS, R., HUTCHINS, N. & MARUSIC, I. 2009 Large-scale amplitude modulation of the small-scale structures in turbulent boundary layers. *J. Fluid Mech.* **628**, 311–337.

MCKEON, B. J. & SHARMA, A. S. 2010 A critical layer model for turbulent pipe flow. *J. Fluid Mech.* **658**, 336–382.

MONTY, J. P., HUTCHINS, N., NG, H. C. H., MARUSIC, I. & CHONG, M. S. 2009 A comparison of turbulent pipe, channel and boundary layer flows. *J. Fluid Mech.* **632**, 431–442.

MONTY, J. P., STEWART, J. A., WILLIAMS, R. C. & CHONG, M. S. 2007 Large-scale features in turbulent pipe and channel flows. *J. Fluid Mech.* **589**, 147–156.

MORRISON, J. F., MCKEON, B. J., JIANG, W. & SMITS, A. J. 2004 Scaling of the streamwise velocity component in turbulent pipe flow. *J. Fluid Mech.* **508**, 99–131.

NOLAN, K. P. & ZAKI, T. A. 2013 Conditional sampling of transitional boundary layers in pressure gradients. *J. Fluid Mech.* **728**, 306–339.

POPE, S. B. 2000 *Turbulent Flows*. Cambridge University Press.

SCHLATTER, P., LI, Q., BRETHOUWER, G., JOHANSSON, A. V. & HENNINGSON, D. S. 2010 Simulations of spatially evolving turbulent boundary layers up to $Re_\theta = 4300$. *Intl J. Heat Fluid Flow* **31**, 251–261.

SHARMA, A. S. & MCKEON, B. J. 2013 On coherent structure in wall turbulence. *J. Fluid Mech.* **728**, 196–238.

SIMENS, M. P., JIMÉNEZ, J., HOYAS, S. & MIZUNO, Y. 2009 A high-resolution code for turbulent boundary layers. *J. Comput. Phys.* **228**, 4218–4231.

SMITS, A. J., MCKEON, B. J. & MARUSIC, I. 2011 High-Reynolds number wall turbulence. *Annu. Rev. Fluid Mech.* **43**, 353–375.

TOMKINS, C. D. & ADRIAN, R. J. 2003 Spanwise structure and scale growth in turbulent boundary layers. *J. Fluid Mech.* **490**, 37–74.

VALLIKIVI, M., HULTMARK, M., BAILEY, S. C. C. & SMITS, A. J. 2011 Turbulence measurements in pipe flow using a nano-scale thermal anemometry probe. *Exp. Fluids* **51** (6), 1521–1527.

ZHOU, J., ADRIAN, R. J., BALACHANDAR, S. & KENDALL, T. M. 1999 Mechanisms for generating coherent packets of hairpin vortices in channel flow. *J. Fluid Mech.* **387**, 353–396.